A nonlinear numerical model for comparative study of gravity wave propagation in planetary atmospheres

Sarthak Srivastava[1], Amal Chandran[1], and Edward Michael Benjamin Thiemann[2]

[1]Nanyang Technological University
[2]Laboratory for Atmospheric and Space Physics

November 21, 2022

Abstract

A two-dimensional nonlinear numerical model has been developed to study atmospheric coupling due to vertically propagating Gravity Waves (GWs) on different planets. The model is able to simulate both acoustic and gravity waves due to inclusion of compressibility. The model also considers dissipative effects due to viscosity, conduction and radiative damping. The hyperbolic inviscid advection equations are solved using the Lax-Wendroff method. The parabolic diffusion terms are solved implicitly using a linear algebra-based Direct method. The model is validated by comparing numerical solutions against analytical results for linear propagation, critical level absorption and breaking. A case study of tsunami-generated GWs is presented for the 2004 Sumatra earthquake whereby the model is forced through tsunamigenic sea-surface displacement. The properties of simulated GWs closely match those derived from ionospheric sounding observations reported in literature. Another application for Martian ice cloud formation is discussed where GWs from topographic sources are shown to create cold pockets with temperatures below the CO2 condensation threshold. The simulated cold pockets coincide with the cloud echo observations from the Mars Orbiting Laser Altimeter (MOLA) aboard Mars Global Survey (MGS) spacecraft.

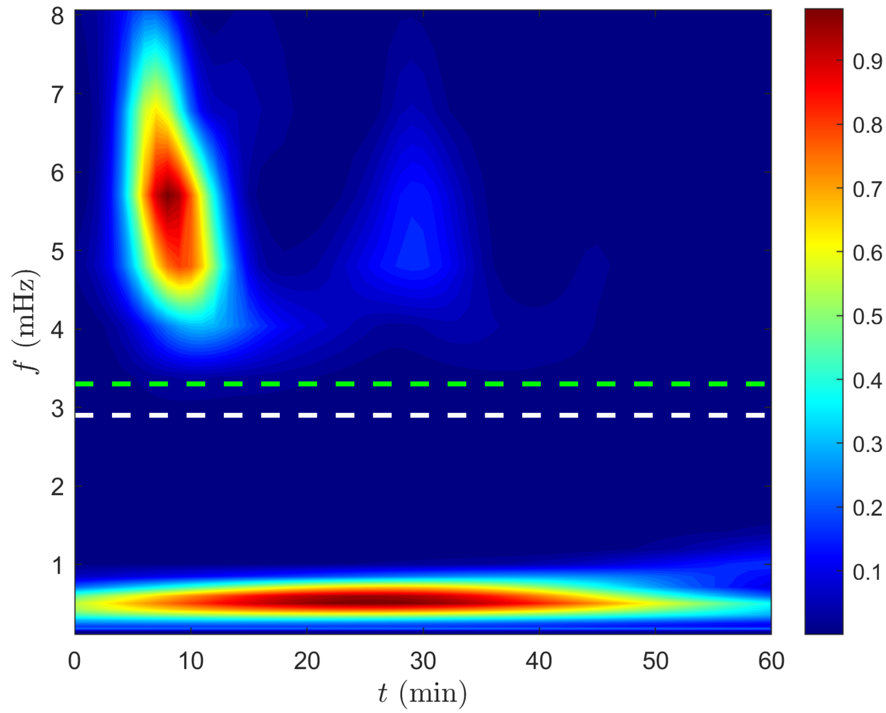

0.9
0.8
0.7
0.6
0.5
0.4
0.3
0.2
0.1
f (mHz)
t (min)

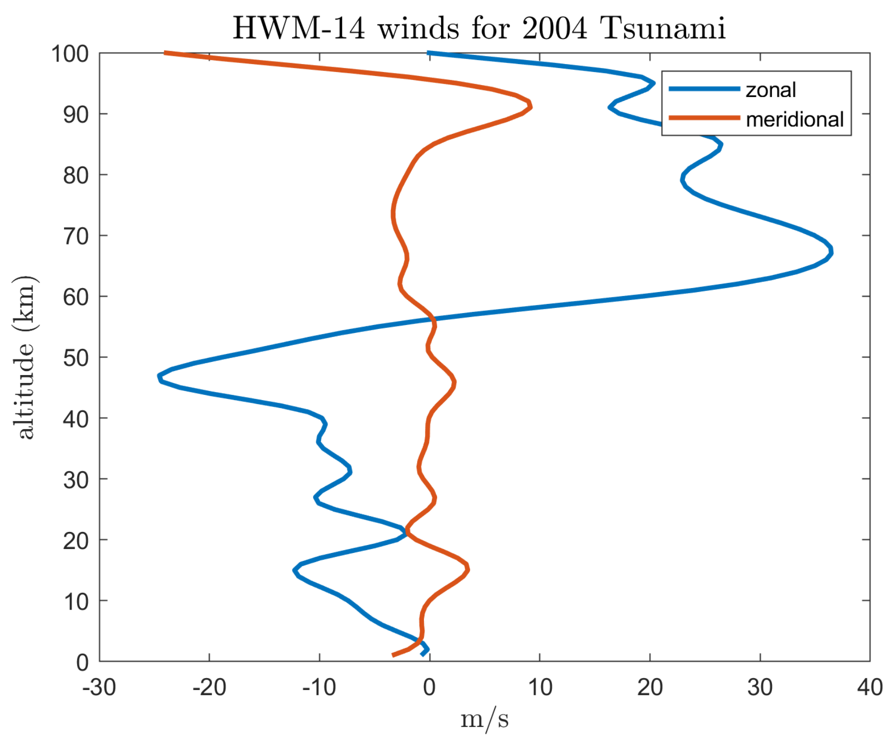

HWM-14 winds for 2004 Tsunami
zonal
meridional
altitude (km)
m/s

A nonlinear numerical model for comparative study of gravity wave propagation in planetary atmospheres

Sarthak Srivastava[1], Amal Chandran[1,2], Edward M. B. Thiemann[2]

[1]Satellite Research Centre, School of EEE, Nanyang Technological University, Singapore
[2]Laboratory for Atmospheric and Space Physics, University of Colorado at Boulder, USA

Key Points:

- A two-dimensional nonlinear compressible model is presented for simulation of Gravity Waves (GWs) in different planetary atmospheres.
- The model is validated against analytical predictions, and 2 applications on Earth and Mars, respectively are discussed.
- The model is well-suited to perform comparative studies of GW propagation, growth, and dissipation on different planets.

Corresponding author: Sarthak Srivastava, `sarthak002@e.ntu.edu.sg`

Abstract

A two-dimensional nonlinear numerical model has been developed to study atmospheric coupling due to vertically propagating Gravity Waves (GWs) on different planets. The model is able to simulate both acoustic and gravity waves due to inclusion of compressibility. The model also considers dissipative effects due to viscosity, conduction and radiative damping. The hyperbolic inviscid advection equations are solved using the Lax-Wendroff method. The parabolic diffusion terms are solved implicitly using a linear algebra-based Direct method. The model is validated by comparing numerical solutions against analytical results for linear propagation, critical level absorption and breaking. A case study of tsunami-generated GWs is presented for the 2004 Sumatra earthquake whereby the model is forced through tsunamigenic sea-surface displacement. The properties of simulated GWs closely match those derived from ionospheric sounding observations reported in literature. Another application for Martian ice cloud formation is discussed where GWs from topographic sources are shown to create cold pockets with temperatures below the CO2 condensation threshold. The simulated cold pockets coincide with the cloud echo observations from the Mars Orbiting Laser Altimeter (MOLA) aboard Mars Global Survey (MGS) spacecraft.

Plain Language Summary

Gravity Waves (GWs) are oscillations in the atmosphere that are responsible for a variety of effects related to disturbances in wind patterns and changes in plasma in the upper atmosphere. These effects are important enough that GWs need to be properly accounted for in the climate models of planets. However, the typical wavelengths of GWs are much smaller than the typical resolutions of these climate models leaving no choice but to use limited approximations. Several models have been developed independently to perform detailed computer simulations of GWs on different planets, differing in their capabilities and limitations. There is a lack of a general model that can be used to simulate GWs on any planetary atmosphere.

Here we present such a model that can be very useful for performing comparison studies of GWs on different planets. We present the model equations and solution methods. We then validate the model by showing agreement between simulations and predictions from theory. We then apply our model to 2 case studies: simulating GWs from the 2004 Sumatra tsunami, and identifying regions of CO_2 ice cloud formation on Mars. Results from both the case studies agree with the observation data published in previous studies.

1 Introduction

Gravity Waves (GWs) play an important role in atmospheric dynamics. By acting as an effective coupling mechanism, GWs are responsible for upward and long-range transport of energy and momentum from various sources. Momentum deposition by GWs is responsible for several planetary atmospheric variabilites not explained by radiative equilibrium alone. For example, GWs result in reversal of mean meridional temperature gradient in Earth's mesosphere and phenomena such as Quasi Biennial Oscillation (Andrews et al., 1987). On Mars, GWs are shown to create cold pockets leading to formation of CO_2 ice clouds (Yiğit et al., 2015). Large stationary gravity waves due to orographic forcing have been reported on Venus (Lefèvre et al., 2020). Asymmetric sub-solar to anti-solar circulation on Venus is also attributed to momentum deposition by GWs (Sánchez-Lavega et al., 2017). Upward propagating GWs lead to thermal effects at higher altitudes (Hickey et al., 2000), (A. S. Medvedev et al., 2015) and cause plasma density perturbations upon reaching ionospheric heights. Such ionospheric disturbances have been extensively studied on Earth (Hocke et al., 1996), Mars (England et al., 2017), Jupiter (Matcheva et al., 2001) and Saturn (Barrow & Matcheva, 2013). There is a need for comparative study of these fast-moving, small-scale waves that exert significant influence on atmospheric dynamics.

To accurately simulate the atmospheric dynamics and climate on planets, physics-based Global Circulation Models (GCMs) of differing complexity have been developed which numerically solve the non-linear fluid equations. To obtain realistic results, these GCMs must incorporate gravity wave dynamics. However, wave scales being much smaller than typical GCM resolutions means that gravity wave effects are included in many GCMs through approximate parameterizations (e.g. reviews by Alexander et al. (2010); Kim et al. (2003) etc.). These parameterizations result in unrealistic representations of gravity waves due to the simplifications involved. Thus, numerical modelling is needed to properly characterize the propagation and effects of GWs (Gavrilov & Kshevetskii, 2014; Snively & Pasko, 2008; Franke & Robinson, 1999; Yu & Hickey, 2007; Brissaud et al., 2016). To understand the effect of planetary characteristics on wave evolution and propagation, wave modeling from fundamental principles is needed for different planets. Several such modeling studies have been performed for other planets, for example, Mars (Barnes, 1990; Parish et al., 2009), Venus (McGouldrick & Toon, 2008; Baker et al., 2000), Jupiter (Hickey et al., 2000), Saturn (Barrow & Matcheva, 2013), Pluto (Cheng et al., 2017), and even exoplanet HD 209458 b (Watkins & Cho, 2010). These studies have been performed in isolation using models specific to different planets. There is a need to comparatively quantify propagation, growth and dissipation of GWs due to differing ambient planetary atmospheric conditions. This requires a flexible modeling approach such that the same model formulation can extend to other planetary regimes.

Study of GW dynamics as a result of varying planetary atmospheric conditions would require computations across a large parameter space of atmospheric variables. This highlights a need for simplified models for comparative GW studies across different planets. Simplified models are very useful in performing controlled numerical experiments in order to gain physical insight. This approach has been widely popular in atmospheric modeling of exoplanets (Kaspi & Showman, 2015; Read et al., 2018). Models of GW propagation must also incorporate nonlinear dynamics to adequately describe wave-flow interactions and saturation processes (Franke & Robinson, 1999). These processes are responsible for selective wave filtering and momentum deposition (Fritts & Alexander, 2003). These processes are difficult to describe analytically without making drastically simplifying assumptions. This makes numerical modeling an indispensable tool for their study.

In this paper, we present MAGNUS-P (Model for Acoustic Gravity wave Numerical Simulation in Planetary atmospheres): a two-dimensional, nonlinear, compressible planetary atmospheric GW model. This model is capable of simulating both acoustic and gravity waves due to inclusion of compressibility. The model is based on second order finite difference formulation of conservative fluid equations in two dimensions with inclusion of viscous and thermal dissipation. By varying the background atmospheric state, MAGNUS-P can be used to quantify propagation, growth and dissipation of GWs across different planets. This makes the model very useful for performing fast iterations for parametric studies. As a modular wave propagation solver, MAGNUS-P can be coupled with separate wave forcing models and with electrodynamics models to simulate ionospheric effects of GWs. This model was developed to be used for studying GW propagation in Mesosphere and Lower Thermosphere (MLT) region on Earth, and for comparative wave simulations on Venus and Mars.

2 MAGNUS-P: Model for Acoustic Gravity wave Numerical Simulation in Planetary atmospheres

In this section, we present the equations and implementation behind our atmospheric gravity wave model, MAGNUS-P. We discuss the governing equations, solution methods and boundary conditions.

2.1 Governing equations

Fluid motion is governed by the Navier-Stokes equations. These equations without viscous terms, called Euler equations, are written in conservative form for two-dimensional, compressible, fully nonlinear case with gravity as (LeVeque, 2002):

$$\frac{\partial \rho}{\partial t} + \nabla \cdot (\rho \vec{v}) = 0 \tag{1}$$

$$\frac{\partial (\rho \vec{v})}{\partial t} + \nabla \cdot (\rho \vec{v} \vec{v}) = -\nabla p - \rho \vec{g} \tag{2}$$

$$\frac{\partial E}{\partial t} + \nabla \cdot ((E + p)\vec{v}) = -\rho \vec{g} \vec{v} + \rho q \tag{3}$$

Here ρ is density, $\vec{v}$ is velocity, p is pressure, E is specific energy and q is thermodynamic heating. Eq. (1) describes conservation of mass, Eq. (2) describes conservation of momentum, and Eq. (3) describes the conservation of energy. Definition of specific energy, E follows from the equation of state which closes this set of equations:

$$E = \frac{p}{\gamma - 1} + \frac{1}{2}\rho(\vec{v} \cdot \vec{v}) \tag{4}$$

These equations form a set of hyperbolic Partial Differential Equations (PDEs), which can be written for 2-D as:

$$\frac{\partial Q}{\partial t} + \frac{\partial F(Q)}{\partial x} + \frac{\partial G(Q)}{\partial z} = S(Q) \tag{5}$$

such that $Q = \begin{bmatrix} \rho \\ \rho u \\ \rho w \\ E \end{bmatrix}$, flux terms $F = \begin{bmatrix} \rho u \\ \rho u^2 + p \\ \rho u w \\ u(E + p) \end{bmatrix}$, and $G = \begin{bmatrix} \rho w \\ \rho u w \\ \rho w^2 + p \\ w(E + p) \end{bmatrix}$, and the source term $S = \begin{bmatrix} 0 \\ 0 \\ -\rho g \\ -\rho g w + \rho q \end{bmatrix}$, where u and w are horizontal and vertical components of velocity, respectively. The molecular viscosity equation can be written as (Pitteway & Hines, 1963):

$$\frac{\partial \vec{v}}{\partial t} = \nu \nabla^2 \vec{v} + \frac{\nu}{3} \nabla(\nabla \cdot \vec{v}) \tag{6}$$

where ν is kinematic viscosity (also called momentum diffusivity). Vadas and Fritts (2005) have shown that the second term in Eq. (6) is negligible for vertically propagating GWs with vertical wavelengths $\lambda_z << 4\pi H$, with H being the atmospheric scale height.

Thus, the equation for molecular viscosity is simplified as :

$$\frac{\partial \vec{v}}{\partial t} = \nu \nabla^2 \vec{v} \tag{7}$$

Dissipation due to thermal conduction is given by a similar diffusion equation:

$$\frac{\partial T}{\partial t} = \alpha \nabla^2 T \tag{8}$$

where α is thermal diffusivity, which is related to ν through Prandtl number, $Pr = \frac{\nu}{\alpha}$.

2.2 Computational solution

The two-dimensional model equations are solved using finite difference methods. Advective terms and diffusive terms are solved separately due to their different respective PDE forms. In this section, we formulate the discretized equations used in the model.

2.2.1 Model domain

The discretized numerical domain is illustrated in Fig. 1. A rectangular grid is used with two ghost cells surrounding the computational domain for enforcing boundary conditions. There is a total of I grid points in x and J grid points in z. Horizontal grid resolution is denoted by Δx and vertical resolution by Δz. Provision is made for an optional sponge layer at the model top to absorb outgoing waves and prevent spurious reflections.

images/Model_domain.JPG

Figure 1. Illustration of discretized 2-D model domain. i and j refer to x (horizontal) and z (vertical) cell indices. The computational domain (blue) is surrounded by 2 ghost cells (green) on all the sides. A sponge layer is additionally implemented at the model top.

2.2.2 Advective solution

The 2-D hyperbolic Euler equation system (5) is solved using the 2-step Richtmeyer Lax-Wendroff method in a dimensionally-split fashion (LeVeque, 2002). Letting i, j be the grid indices in x and z directions respectively and n being the time index, Lax-Wendroff 2-step solution in x-direction is computed first using:

$$\begin{aligned} Q^{n+\frac{1}{2}}_{i+\frac{1}{2},j} &= \frac{1}{2}(Q^n_{i,j} + Q^n_{i+1,j}) - \frac{\Delta t}{2\Delta x}(F^n_{i+1,j} - F^n_{i,j}), \\ Q^{n+1}_{i,j} &= Q^n_{i,j} - \frac{\Delta t}{\Delta x}(F^{n+\frac{1}{2}}_{i+\frac{1}{2},j} - F^{n+\frac{1}{2}}_{i-\frac{1}{2},j}) \end{aligned} \tag{9}$$

where $F^{n+\frac{1}{2}}_{i+\frac{1}{2},j}$ refers to flux term recomputed for $Q^{n+\frac{1}{2}}_{i+\frac{1}{2},j}$. After enforcing boundary conditions, the solution in z-direction is computed using:

$$\begin{aligned} Q^{n+\frac{1}{2}}_{i,j+\frac{1}{2}} &= \frac{1}{2}(Q^n_{i,j} + Q^n_{i,j+1}) - \frac{\Delta t}{2\Delta z}(G^n_{i,j+1} - G^n_{i,j}) + \frac{\Delta t}{2}S^n_{i,j}, \\ Q^{n+1}_{i,j} &= Q^n_{i,j} - \frac{\Delta t}{\Delta z}(G^{n+\frac{1}{2}}_{i,j+\frac{1}{2}} - G^{n+\frac{1}{2}}_{i,j-\frac{1}{2}}) + \frac{\Delta t}{2}(S^{n+\frac{1}{2}}_{i,j+\frac{1}{2}} + S^{n+\frac{1}{2}}_{i,j-\frac{1}{2}}) \end{aligned} \tag{10}$$

where vertical flux term $G^{n+\frac{1}{2}}_{i,j+\frac{1}{2}}$ and source term $S^{n+\frac{1}{2}}_{i,j+\frac{1}{2}}$ are recomputed for intermediate step prognostic term $Q^{n+\frac{1}{2}}_{i,j+\frac{1}{2}}$. This numerical scheme is second order accurate in both space and time. Numerical stability of the solution method is dependent on the Courant-Friedrich-Lewy (CFL) condition such that

$$CFL = \frac{v_{max}\Delta t}{\min(\Delta x, \Delta z)} < 1 \tag{11}$$

where v_{max} is the maximum flow speed anywhere in the domain. The timestep Δt for advective solution is adaptively computed to satisfy the CFL condition.

2.2.3 Diffusion solution

The equations for molecular viscosity and thermal conduction (Eqs. (7) and (8)) are diffusion-type PDEs with the general form:

$$\frac{\partial u}{\partial t} = \kappa \nabla^2 u \tag{12}$$

where u is the quantity to be solved for ($\vec{v}$ in Eq. (7) and T in Eq. (8)), and κ denotes the diffusion coefficient (ν in Eq. (7) and α in Eq. (8)). Using Forward Euler in time and Centered Differences in space, this equation can be discretized to yield an explicit solution for $u^{n+1}_{i,j}$ as:

$$u^{n+1}_{i,j} = u^n_{i,j} + f_x(u^n_{i+1,j} - 2u^n_{i,j} + u^n_{i-1,j}) + f_z(u^n_{i,j+1} - 2u^n_{i,j} + u^n_{i,j-1}) \tag{13}$$

Where $f_x = \frac{\kappa\Delta t}{(\Delta x)^2}$ and $f_z = \frac{\kappa\Delta t}{(\Delta z)^2}$ are mesh Fourier numbers. For stability, it is required that $f_x < \frac{1}{2}$ and $f_z < \frac{1}{2}$ (LeVeque, 2002). In vertical direction this implies:

$$\frac{\kappa\Delta t}{(\Delta z)^2} < \frac{1}{2} \implies \Delta t < \frac{(\Delta z)^2}{2\kappa} \tag{14}$$

Exponentially decreasing density with increasing height results in very low values of κ (Sanchez-Lavega, 2010), which make the necessary solution timestep Δt too small. This makes the solution impractical due to the huge computation time required. Using representative vertical profiles of molecular viscosity for Earth, Venus, Mars (refer to appendix Appendix A) and assuming $\Delta z = 0.5$ km, minimum timestep required for solution of Eq. (12) using the explicit method is shown in Fig. 2.

images/Min_timestep_visc.png

Figure 2. Minimum timestep required for stable solution of viscous dissipation using the explicit method for grid size $\Delta z = 0.5$ km. Minimum timestep required becomes very low above $\sim$ 100 km altitude, leading to impractically long computational times.

Thus, explicit solution of the diffusion equations using Eq. (13) is not feasible and an implicit approach is desired. Using Crank-Nicholson scheme, Eq. (12) is discretized to yield the following implicit expression for $u_{i,j}^{n+1}$:

$$\begin{aligned}\frac{u_{i,j}^{n+1} - u_{i,j}^{n}}{\Delta t} = \frac{k}{2}\left(\frac{u_{i+1,j}^{n+1} - 2u_{i,j}^{n+1} + u_{i-1,j}^{n+1}}{(\Delta x)^2} + \frac{u_{i+1,j}^{n} - 2u_{i,j}^{n} + u_{i-1,j}^{n}}{(\Delta x)^2}\right) + \\ \frac{k}{2}\left(\frac{u_{i,j+1}^{n+1} - 2u_{i,j}^{n+1} + u_{i,j-1}^{n+1}}{(\Delta z)^2} + \frac{u_{i,j+1}^{n} - 2u_{i,j}^{n} + u_{i,j-1}^{n}}{(\Delta z)^2}\right)\end{aligned} \tag{15}$$

Letting $\Delta x = \Delta z$ (uniform grid), we define the mesh Fourier number as $f = \frac{\kappa \Delta t}{(\Delta x)^2}$. Eq. (15) can be rearranged to yield a linear system of the form (Langtangen & Linge, 2017):

$$\mathbf{A}\mathbf{x} = \mathbf{B} \tag{16}$$

Here the unknown $\mathbf{x}$ is the solution vector of size $(I \times J) \times 1$ containing $u_{i,j}^{n+1}$ values for all grid points (i.e. for all i, j combinations). $\mathbf{B}$ is size $(I \times J) \times 1$ vector containing the previous timestep solution, $u_{i,j}^{n}$ for all grid points. Thus,

$$\mathbf{x} = \begin{bmatrix} u_{1,1}^{n+1} \\ u_{1,2}^{n+1} \\ \vdots \\ u_{1,J}^{n+1} \\ u_{2,1}^{n+1} \\ \vdots \\ u_{I,J}^{n+1} \end{bmatrix}, \quad \mathbf{B} = \begin{bmatrix} u_{1,1}^{n} \\ u_{1,2}^{n} \\ \vdots \\ u_{1,J}^{n} \\ u_{2,1}^{n} \\ \vdots \\ u_{I,J}^{n} \end{bmatrix} \tag{17}$$

The coefficient matrix $\mathbf{A}$ is a sparse matrix of size $(I \times J) \times (I \times J)$ with 5 diagonals. Construction of $\mathbf{A}$ requires flattening the 2-D $I \times J$ model domain into a vector of size $(I \times J) \times 1$ (Langtangen & Linge, 2017). We define $a = 1 + \frac{2\kappa}{(\Delta x)^2}$ and $c = \frac{-\kappa}{(2\Delta x)^2}$. The central (or zeroth) diagonal of $\mathbf{A}$ is populated with a, the $+I^{th}$ and $-I^{th}$ diagonals are populated with c, and +1 and -1 diagonals are populated with $I \times 1$ vector $[0, c, c, c, ...]^T$ repeated $J-1$ times.

$$\mathbf{A} = \begin{bmatrix} a & c & 0 & 0 & \dots & c & 0 & \dots & 0 & 0 \\ c & a & c & 0 & \dots & 0 & c & \dots & 0 & 0 \\ 0 & c & a & c & \dots & 0 & 0 & \dots & 0 & 0 \\ \vdots & & & \ddots & & & \ddots & & & \vdots \\ c & 0 & 0 & 0 & \dots & 0 & 0 & \dots & 0 & 0 \\ 0 & c & 0 & 0 & \dots & a & 0 & \dots & 0 & 0 \\ \vdots & & & \ddots & & & \ddots & & & \vdots \\ 0 & 0 & 0 & 0 & \dots & 0 & 0 & \dots & c & 0 \\ 0 & 0 & 0 & 0 & \dots & 0 & 0 & \dots & a & c \\ 0 & 0 & 0 & 0 & \dots & 0 & 0 & \dots & c & a \end{bmatrix} \tag{18}$$

The matrix system in Eq. (16) is solved directly using LU factorization. Solution of diffusion equation using this implicit approach has a major advantage of being unconditionally stable regardless of the timestep size.

2.2.4 Boundary conditions

The horizontal Boundary Conditions (BCs) are set to periodic, which makes the model horizontal extent equal to the horizontal wavelength. This feature is useful for setting the desired horizontal wavelength of the forced waves. Referring to Fig. 1, periodic BCs are enforced by setting the following:

$$Q^n_{1,j} = Q^n_{I-3,j}, \quad Q^n_{2,j} = Q^n_{I-2,j}, \quad Q^n_{I-1,j} = Q^n_{3,j}, \quad Q^n_{I,j} = Q^n_{4,j} \tag{19}$$

Closed (reflective) condition is implemented at the bottom while the model top is set to outflow boundary condition. Zero order extrapolation scaled with density is applied for outflow condition to account for atmospheric stratification (LeVeque, 2002):

$$Q^n_{i,j+1} = \bar{Q}^n_{i,j+1} + Q'_{i,j}\sqrt{\frac{\bar{\rho}_{i,j+1}}{\bar{\rho}_{i,j}}},\ Q^n_{i,j+2} = \bar{Q}^n_{i,j+2} + Q'_{i,j}\sqrt{\frac{\bar{\rho}_{i,j+2}}{\bar{\rho}_{i,j}}}, \tag{20}$$

where the overbar refers to background quantity and prime refers to the perturbation. The model can be forced by specifying vertical velocity profile at the lower boundary condition or alternatively, by specifying thermal forcing.

2.2.5 Radiative damping

Radiative damping due to CO_2 15 μm band is significant in Martian and Venusian middle atmospheres due to their CO_2 dominant composition. Radiative damping is vertical scale dependent and dominates dissipation due to molecular viscosity below ∼120 km altitude on Mars and above ∼100 km altitude on Venus (Imamura & Ogawa, 1995). For realistic modelling of GWs, it is important to include the role of CO_2 infrared radiative damping in limiting wave amplitude growth on Mars and Venus.

The radiative damping time scale, τ_r, refers to the time taken for a thermal disturbance to decay by a factor of $1/e$ (Crisp, 1989). The reciprocal of damping time scale, known as damping rate (τ^{-1}) is estimated using the method described by Eckermann et al. (2011). Based on Curtis-matrix based modeling, Eckermann et al. (2011) provide lookup coefficients to estimate CO_2 15 μm radiative damping rates for different vertical wavenumbers. The lookup coefficients can be used to estimate damping rates for vertical wavelengths in the range 1-500 km, up to an altitude of 200 km. According to Eckermann et al. (2011), the damping rate is given by

$$\tau_r^{-1}(z, m) = \exp(a(z) + b(z)\psi + c(z)\psi^2 + d(z)\psi^3) \tag{21}$$

where

$$\psi = \ln m - \ln \frac{2\pi}{500} \tag{22}$$

Here z is altitude (in km), m is vertical wavenumber (in km^{-1}) and $a(z)$, $b(z)$, $c(z)$, $d(z)$ are lookup coefficients. The estimated $\tau_r^{-1}(z, m)$ corresponds to a provided reference temperature profile over vertical grid from $z = 0$ to 200 km with 0.5 km spacing. For any arbitrary temperature profile, damping rates can be scaled from the reference values using the following relation:

$$\frac{\tau_r^{-1}}{\frac{\partial \theta}{\partial t}} = \frac{\tau_r^{-1}}{\frac{\partial \theta}{\partial t}}|_{ref} \tag{23}$$

where

$$\frac{\partial \theta}{\partial t} = 1.23686 \times 10^5 \times \frac{\exp{(971/T)}}{T^2(\exp(971/T) - 1)^2} \tag{24}$$

Radiative damping length scale is defined as (Hinson & Jenkins, 1995):

$$L_r = 2|\frac{\hat{\omega}}{m}|\tau_r \tag{25}$$

If the radiative damping length scale is much greater than the scale height ($L_r >> 2H$) or the damping time scale is much greater than the wave period ($\tau_r >> \tau$), the effect of damping due to radiation can be regarded as insignificant.

Radiative damping is implemented in the model in a similar fashion to Newtonian cooling, using the following equation (Fels, 1982):

$$\frac{\partial T}{\partial t} = -\frac{T^{'}}{\tau_r} \tag{26}$$

where $T^{'}$ is temperature perturbation. This equation is discretized using Crank-Nicholson scheme to yield the following explicit expression:

$$T_{i,j}^{n+1} = \frac{(1 - \frac{\Delta t}{2\tau_r})T_{i,j}^n + T_a\frac{\Delta t}{\tau_r}}{(1 + \frac{\Delta t}{2\tau_r})} \tag{27}$$

where T_a refers to the background temperature.

3 Model validation

In this section, we validate our model by simulating 3 test cases, corresponding to linear wave propagation, critical layer absorption and breaking. The simulation results are compared against analytical predictions. For validation purposes, we utilize an Earth isothermal atmosphere with $T = 290$ K, and density and pressure decreasing exponentially with height in altitude range 0-160 km. Kinematic viscosity profile is adapted from Banks and Kockarts (2013):

$$\nu(z) = 3.5 \times 10^{-7} T(z)^{0.69}/\rho(z) \tag{28}$$

3.1 Linear dispersion relation

The vertical velocity forcing at the lower boundary is of the form:

$$w(x, z = 0, t) = \tilde{w}\cos(\omega(t - t_0) - kx)\exp\left(-\frac{(t - t_0)^2}{2\sigma_t^2}\right) \tag{29}$$

Isothermal background atmosphere is used and simulation variables are listed in table 1.

Table 1. Simulation parameters for validation with linear theory.

$\tilde{w}$	t_0	σ_t	ω	λ_x	dx	dz	CFL
0.001 m/s	1200 s	600 s	0.007 rad/s	40 km	0.5 km	0.5 km	0.8

Magnitude of forcing is kept small to ensure linear wave regime to enable comparisons with linear wave theory. No dissipation is modelled for validation with linear theory, however a 20 km sponge layer is implemented above the domain to prevent spurious oscillations.

We plot the density-scaled vertical velocity, $w\sqrt{\frac{\rho}{\rho_0}}$, profiles at the middle of the horizontal model domain with time. This results in a wave travel diagram illustrating propagation trends over time, as shown in Fig. 3(a). It is seen that the wave travels without overturning or breaking. Gravity wave dispersion relation for frequencies (ω) much higher than Coriolis frequency (f), i.e. $\omega >> f$, is given by Fritts and Alexander (2003):

$$\omega = \frac{Nk}{\sqrt{k^2 + m^2}} \tag{30}$$

Here, Brunt-Visl frequency, $N = \sqrt{\gamma - 1}\frac{g}{c_s}$ is taken to be 0.0182 rad/s, k and m are the horizontal and vertical wavenumbers, respectively. From the dispersion relation, we obtain $m = 3.77{\times}10^{-4}m^{-1}$ which equates to vertical wavelength, λ_z = 16.7 km. From simulation results, we compute the wavelet transform of density-scaled vertical velocity profiles, $w\sqrt{\frac{\rho}{\rho_0}}$ for x in the middle of the horizontal domain obtained from simulation results. We compute the wavelet power spectrum and divide by the maximum power to yield the normalized spectrum for each profile. The normalized wavelet spectrum profiles after 30 min of simulation start time are plotted in Fig. 3(b). We observe dominant $\lambda_z \sim 16.8$ km based on the peak wavelet power. This agrees very well with the prediction from linear dispersion relation. Also, the vertical wavelength is observed to remain constant with time due to absence of dissipation.

3.2 Critical layer

We use our model to simulate gravity wave interaction with mean flow leading to critical level absorption. Model forcing is identical to the settings mentioned in section 3.1. However, we add a horizontal background wind in this case. We simulate a Gaussian wind profile varying vertically according to:

$$\bar{u}(z) = u_0 \exp\left(-\frac{(z - z_0)^2}{2\sigma_u^2}\right) \tag{31}$$

The parameter for background wind are such that u_0 = 100 m/s, z_0 = 100 km, and σ_u = 10 km. The maximum wind speed u_0 is set high enough to exceed the phase wave speed.

Fig. 4(a) shows the wave travel diagram for critical filtering case. It is seen that the wave packets are abruptly terminated below 90 km, unable to propagate upwards. Fig. 4(b) shows scaled vertical velocity contour after 5000 s of simulation time. We show 2 sample vertical velocity profiles in Fig. 5. The Gaussian background wind is also plotted (dashed grey line) to identify the wind velocity and corresponding altitude where the critical layer exists. According to theory, critical level exists when horizontal phase speed equals the mean wind speed, i.e. $c_x = \bar{u}$. Given $c_x = \frac{\omega}{k}$, the horizontal phase speed is estimated to be 44.6 m/s. From simulation, we identify critical level to be around z = 88.3 km and the corresponding value of $\bar{u}$ at this height is 44.4 m/s. This is very close to the estimated phase speed from theory, and hence validates the simulated result.

images/WTD_dispersion.png

Figure 3. (a) Wave travel diagram showing linear GW propagation. (b) Normalized wavelet power for vertical wavelength at various simulation times (starting after $t = 1800$ s). Based on peak power, the dominant $\lambda_z = 16.8$ km throughout.

3.3 Breaking

We use our model to simulate a wave breaking instance by ensuring departure from linear behaviour. Linear convective instability demands the ratio $\frac{u^{'}}{(c-u)} = 1$, where $u^{'}$ is horizontal wind perturbation. However in practise, this ratio is found to be ~ 0.7 (Fritts et al., 1988). Using theoretical consideration of nonlinear diffusion, A. Medvedev and Klaassen (2000) find this ratio to be 0.707. We increase the convective instability ratio by increasing the forcing amplitude $\tilde{w}$ in Eq. (29) to a much larger value of 1 m/s. This ensures wave steepening and earlier onset of breaking. No background wind is simulated in this case. The rest of the simulation parameters remain the same as in table 1.

Richardson number is a common indicator of wave instability, defined as (Nappo, 2013):

$$Ri = \frac{N^2}{(\frac{\partial u}{\partial z})^2} \tag{32}$$

images/WTD_criticallayer.png

Figure 4. (a) Wave travel diagram for critical layer case. Waves do not propagate vertically above $z = 88.3$ km . (b) Scaled vertical velocity contour at $t = 5000$ s demonstrating a critical level interaction of gravity wave with the background wind.

Flow is dynamically unstable when $Ri \leq 0.25$. We calculate the value of Ri everywhere in the computational domain and mark regions where $Ri \leq 0.25$ on the wave travel diagram. Fig. 6(a) shows the wave travel diagram with white overlaid contours where instability is expected from Ri consideration. The waves are seen to break around $t = 5000$ s, exactly corresponding to the white contours depicting Ri threshold. A scaled vertical velocity X-Z plot at $t = 5000$ s in Fig. 6(b) clearly shows waves breaking into turbulent eddies at $z \sim 80$ km.

4 Model applications

The previous section demonstrated validation of MAGNUS-P model with results from linear theory of gravity waves. Simulations of wave-mean flow interaction and wave breaking were also shown to agree with theoretical predictions. In real atmospheres, there are dissipative processes that act to limit the amplitude growth of GWs at higher altitudes, leading to saturation. MAGNUS-P considers the two chief damping mechanisms images/validation_criticallevel_profile.pdf

Figure 5. Wind profiles for critical level interaction validation case. Scaled vertical velocity profiles are shown at $t = 5000$ s (blue line) and 8000 s (red dashed line). The wave amplitude abruptly goes to zero at $z = 88.3$ km due to background wind shear. The Gaussian background wind (shown in dashed grey) is about 44.4 m/s at this altitude.

relevant for vertically propagating GWs: molecular diffusion and thermal conduction. Thus, MAGNUS-P is suitable for application to real atmospheres. In this section, we apply our model to simulate 2 realistic cases: tsunamigenic GWs on Earth and orographic GWs on Mars.

4.1 Tsunami generated AGWs on Earth

Gravity waves can be generated by ocean tsunami waves that are themselves generated from large undersea earthquakes. These waves occur due to coupling of the atmosphere with ocean surface displacement and are detected in the ionosphere a few hours after the earthquake (Artru et al., 2005; Occhipinti et al., 2006). Here we apply our model to simulate gravity waves resulting from the 2004 Sumatra tsunami. A strong earthquake off Sumatran coast (epicenter: 3.29°N, 95.94°E) on December 26, 2004 at 00:58:53 UTC triggered massive tsunami waves. Traveling Ionospheric Disturbances (TIDs) attributed to acoustic-gravity waves resulting from the tsunami were widely reported (DasGupta et al., 2006; Mikhailova et al., 2016; Liu et al., 2006). Our aim is to demonstrate the flexibility of our model to be able to couple with an external tsunami source model and simulate realistic GWs. Thus, we do not consider the resulting ionospheric effects.

Forcing due to tsunami can be modelled as vertical velocity perturbation due to sea surface displacement. The sea surface displacement is modeled using Airy function (Laughman et al., 2017; Wu et al., 2020) as:

$$h(x) = h_0 A_i(1-x)\left(\frac{x}{2}\right)\exp\left(\frac{2-x}{2}\right) \tag{33}$$

The resulting vertical velocity is given by:

$$w(x) = (\bar{u}-c)\frac{\partial h}{\partial x} = w_0(\bar{u}-c)\exp\left(\frac{2-x}{2}\right)\left[A_i(1-x) - A_i'(1-x)x - A_i(1-x)\left(\frac{x}{2}\right)\right] \tag{34}$$

Here h_0 and w_0 are coefficients to produce peak sea surface displacement ~ 0.5 m and peak vertical velocity ~ 0.85 mm/s respectively (Laughman et al., 2017). A_i is the Airy function, tsunami phase speed c is taken to be 200 m/s and $\bar{u}$ is the wind at sea surface. The modelled sea surface height and vertical velocity forcing is shown in Fig. 7. In this simulation we neglect the background wind, thus $\bar{u} = 0$. Background winds at the epicenter were computed using the Horizontal Wind Model 2014 (HWM-14) (Drob et al., 2015), as shown below in Fig. 8. The horizontal phase speed 200 m/s is found to greatly exceed the background winds, thus justifying the windless atmosphere assumption. The background atmospheric profile is taken from the MSISE-00 model (Picone et al., 2002), for 3.5°N, 96°E on 26-Dec-2004, 02:00 UTC to approximate the event ambient conditions. The simulation domain parameters are given in table 2. A 50-km thick sponge layer is implemented above 200 km altitude to prevent spurious reflections at model top. Dissipation from molecular viscosity and thermal conduction is considered and no eddy viscosity is parameterized. To account for varying chemical composition with height, specific heat (γ) and kinematic viscosity (ν) are computed using the species' number denimages/WTD_breaking.png

Figure 6. (a) Wave travel diagram for wave breaking case. Yellow colored overlaid contours are regions where $Ri < 0.25$. Wave instability sets in around $t = 5000$ s, at $z \sim 80$ km . (b) X-Z snapshot of scaled vertical velocity perturbation at $t = 5000$ s. Eddies forming from breaking waves are seen at $z \sim 80$ km and above.

sities obtained from the MSISE-00 model. Specific heat ratio is computed using a simple weighing (Snively & Pasko, 2008):

$$\gamma = \frac{1.4([O_2] + [N_2]) + 1.67[O]}{[N_2] + [O_2] + [O]} \tag{35}$$

Kinematic viscosity ($m^2 s^{-1}$) is derived using (Rees, 1989):

$$\nu = 1 \times 10^{-7} \times \frac{3.43[N_2] + 4.03[O_2] + 3.9[O]}{[N_2] + [O_2] + [O]} T^{0.69}/\rho \tag{36}$$

Prandtl number, Pr is set as 0.7 (Kundu & Cohen, 2002). Gas constant (in $JK^{-1}kg^{-1}$) is given by $R = 8314/M_r$, where M_r is the mean molecular mass given by

$$M_r = \frac{28[N_2] + 32[O_2] + 16[O]}{[N_2] + [O_2] + [O]} \tag{37}$$

images/tsunami_forcing.png

Figure 7. Sea surface displacement and vertical velocity forcing due to tsunami, immediately after the ramp up phase ($t = 600$ s). The displacement and vertical velocity are modelled based on Eqs. (33) and (34) respectively.

images/tsunami_winds.png

Figure 8. Background winds from HWM-14 for the Tsunami case.

Table 2. Simulation parameters for tsunami study.

X_{max}	dx	Z_{max}	dx	T_{max}	CFL
6000 km	10 km	200 km	0.5 km	3 hrs	0.8

Tsunami induced sea surface displacement is known to produce a spectrum of acoustic-gravity waves. Acoustic waves have frequencies above the acoustic cutoff frequency, $\omega_{ac} = \frac{\gamma g}{2c_s}$, while gravity waves have frequencies lower than Brunt-Vaisala frequency, $N = \frac{\sqrt{(\gamma-1)g}}{c_s}$. We calculate $\omega_{ac} \sim 3.3$ mHz and $N \sim 2.9$ mHz. A zero-phase fourth order Butterworth filter with passband 2.9 mHz - 8 mHz is used to isolate acoustic frequencies. Frequency separated time series are plotted for $z = 200$ km in Fig. 9. Acoustic wave peak is seen to arrive slightly under 5 min after simulation start time. This yields a vertical propagation speed of ~ 0.7 km/s for the acoustic waves. This is in close agreement with 0.73 km/s estimated from ionospheric total electron content analysis (Liu et al., 2006; Mikhailova et al., 2016). The gravity mode is filtered with passband 0.1 mHz -2.8 mHz. Gravity wave is much slower and the peak is seen to arrive ~ 90 min after start time. This suggests vertical phase speed of approximately 35 m/s for the GW. We take the time series of sim-

images/tsunami_tseries.png

Figure 9. Vertical velocity time series at $z = 200$ km in the center of model horizontal domain. (Top): unfiltered time series, (Middle): acoustic mode extracted using passband 2.9-8 mHz, (Bottom): gravity mode extracted using passband 0.1-2.8 mHz.

ulated vertical velocity perturbations at $z = 15$ km at the center of model horizontal domain for spectral analysis. Horizontal slice is taken closer to the surface at 15 km altitude to minimize any effects due to dissipation. We apply wavelet analysis to w time series using Morse wavelet (Torrence & Compo, 1998) and plot the normalized wavelet power in Fig. 10. We find peaks at around 5.5 mHz in the acoustic domain and 0.5 mHz in the gravity domain. The acoustic peak is observed much earlier than the slower moving gravity wave. To check the validity of simulated GWs, we compute the vertical phase speed.

images/tsunami_wavelet.png

Figure 10. Normalized wavelet spectrum for frequency filtered w time series at $z = 15$ km. Horizontal white dashed line corresponds to the Brunt-Visl frequency, and the green dashed line is the acoustic cutoff. Wave modes between these two frequencies are evanescent.

Horizontal phase speed given by $c_x = \frac{\omega}{k}$ is known to be 200 m/s. Using $\omega = 0.5$ mHz, we obtain $k = 1.57 \times 10^{-5} m^{-1}$ or $\lambda_x = 400$ km. Using GW dispersion relation in Eq. (30), we calculate the vertical wavenumber, $m = 8.9 \times 10^{-5} m^{-1}$. We now compute the vertical phase speed using $c_z = \frac{\omega}{m}$ to be 35 m/s. This matches the phase speed deduced from time of arrival observation in Fig. 9. Moreover, Laughman et al. (2017) also calculate the dominant horizontal scale of GW to be 400 km and dominant GW period to be 33.3 min or 0.5 mHz, matching our results. This shows that the simulated tsunami driven gravity waves are in good agreement with the predictions from linear theory. Fig. 11 shows the vertical profile of GWs at different times as scaled w contours. The wave amplitude is seen to decrease with altitude due to atmospheric attenuation through viscous damping and thermal conduction.

images/tsunami_result_scaled_w.png

Figure 11. Scaled vertical velocity amplitudes (in m/s) of simulated Tsunamigenic gravity waves at different times. Tsunami source moving to the left is visible. The magnitude of waves is seen to reduce with increasing altitude due to damping caused by molecular viscosity and thermal conduction.

4.2 CO_2 ice cloud formation on Mars

Optically thick clouds over the winter polar caps have been observed by the Mars Orbiting Laser Altimeter (MOLA) aboard the Mars Global Surveyor (MGS) spacecraft. The MOLA cloud observations were obtained from echo returns of 1.06 μm infrared bursts towards the nadir at 0.1 s cadence (Zuber et al., 1992). The observed clouds extend from the surface to 4-6 km above the surface and are found tilted up to 20^o with respect to the background wind. Mountain waves generated by wind flowing over the terrain are suggested as the generating mechanism for these sloping clouds (Pettengill & Ford, 2000). Observational evidence has established that the MOLA-observed clouds form due to CO_2 condensation (Hu et al., 2012).

In this case study, we simulate temperature perturbations due to Martian topographic GWs and compare them with the cloud echoes reported by MOLA. Tobie et al. (2003) performed simulations with cloud microphysics to recreate some of the MOLA cloud echo profiles reported by Pettengill and Ford (2000). Here we use our 2-dimensional nonlinear model to simulate cold pockets caused by topographic GWs to identify regions of possible CO_2 cloud formation. Our interest is limited to generating temperature profiles modulated by gravity waves and thus, no cloud microphysics is included in this modeling study. Horizontal wind over topography can induce perturbations in vertical velocity. This forcing due to flow over topography is given by

$$w(x, t = 0) = \bar{u}\frac{dh(x)}{dx} \tag{38}$$

where $h(x)$ refers to the topography profile. Here we simulate waves from 2 MOLA passes: 207 and 260. The terrain profile for the two passes is taken from Tobie et al. (2003). Density of the background atmosphere is obtained from Mars Climate Database (MCD) v5.3 (Lewis et al., 1999) for solar longitude L_s 316.4° at location 84°N, 72.5°E. Ambient atmosphere at these coordinates realistically represent passes 207 and 260. The background temperature is set to 2% higher than the CO_2 saturation temperature, following Hu et al. (2012). CO_2 saturation temperature profile is taken from Spiga et al. (2012). Background wind is set as constant $\bar{u} = 10$ m/s, which is representative of the Martian winter polar climatology. Furthermore, the wind direction is determined from the slope of the cloud echo observations since the clouds are tilted against the wind (Tobie et al., 2003). The forcing is turned on in a Gaussian ramp up fashion, to minimize acoustic noise. The simulation parameters are summarized in table 3.

Table 3. Simulation parameters for Mars CO_2 cloud study.

X_{max}	dx	Z_{max}	dx	T_{max}	CFL
350 km	0.25 km	15 km	0.25 km	4 hrs	0.85

A sponge layer is implemented to absorb outgoing waves at the model top, i.e. above 15 km (>6 mbar level). No radiative damping or viscous effects are considered in this simulation given small altitudes involved. The model equations are integrated for 4 hours with results stored after every 3 min. Contours of difference between CO_2 condensation temperature (T_{cond}) and simulated temperature (T), are plotted in Fig. 12. Cloud echo data taken from Pettengill and Ford (2000) is overlaid on ($T_{cond}-T$) contours. Nucleation of CO_2 ice particles requires negative temperature perturbations, which are caused by airflow over terrain troughs. Coupled wave dynamics, cloud microphysics and ice particle sedimentation simulations by Tobie et al. (2003) suggest that the nucleation occurs in the upstream of clouds. As the ice particles move with the wind (only a small fraction of ice particles falls to the ground), they grow in size in cold pockets and sublimate in hot pockets, and the associated latent heat provides the damping to prevent resonant trapped wave modes. In Fig. 12, regions with simulated $(T_{cond} - T) > 0$ indicate the cold pockets and vice-versa. Thus, lighter color denotes colder regions and darker color represents warmer pockets. We observe that the overlaid cloud echo observations almost always fall in the coldest pockets, for both pass 207 and 260. The slopes of observed cloud echoes match those of the cold pockets generated by simulation. More cloud echoes are observed just upstream of the relatively warmer pockets, suggesting that nucleation occurs in the upstream of clouds and that the maximum particle size occurs just prior to their moving into the warmer regions (where the particles sublimate). This is consistent with the mechanism put forward by Tobie et al. (2003).

images/clouds207_260.png

Figure 12. Difference between CO_2 condensation temperature and temperature field obtained from topographic GW simulation for MOLA passes 207 and 260. Lighter color is cold and darker color is warmer. The dots indicate cloud echo profiles reported by Pettengill and Ford (2000). The corresponding terrain profiles are reconstructed from Pettengill and Ford (2000) with elevation relative to 6 mbar pressure level. The results are obtained after 4 hours of simulation with background wind, $\bar{u}$ = 10 m/s in direction of increasing x (i.e. left to right).

Airflow along downslope causes adiabatic warming while cooling occurs for flow along upslope. The general warming along a downslope implies that ice clouds can only form above a certain altitude and not too close to the surface. This is evident in the case of pass 207. From Fig. 12 we observe that the terrain for pass 207 has a general downslope from x ∼100 to ∼450 km beyond which the terrain is mostly flat. We observe a global scale warming near the surface and cloud echos are seen to be further from the surface along this downslope region. While modulated by temperature variations caused by surface irregularities, this downslope warming effect is seen to generally hold true. Terrain for pass 260 lacks any large-scale slope, thus general cooling or heating is insignificant. The terrain features result in small-scale wave perturbations leading to development of several finer cold and hot pockets. Despite lacking any condensation microphysics, the temperature fields alone simulated by the model are broadly able to predict the regions of cloud particle nucleation and maximum particle size.

5 Future work and Conclusion

In this paper, we presented MAGNUS-P: a finite difference based 2-D nonlinear compressible numerical model for simulation of acoustic-gravity waves. This wave propagation model can be coupled with separate wave forcing models to simulate waves from different sources. Separate airglow or electrodynamics models can be coupled with MAGNUS-P to simulate the ionospheric effects resulting from the simulated waves. The GW model includes dissipation due to molecular viscosity and thermal conduction, which are important to explain wave saturation at thermospheric heights. Thus, MAGNUS-P can be applied to realistic atmospheres to simulate non-linear wave-mean flow interactions. We have validated the model against results from analytical theory and presented two case studies employing the model to simulate realistic GWs. The first case study presents acoustic-gravity waves from 2004 Sumatra Tsunami simulated using a sea surface height model. Fast moving acoustic waves are seen to arrive at 200 km altitude within 5 min which agrees with the acoustic wave vertical propagation speed deduced from published GNSS TEC studies. Slower gravity waves are observed to arrive at 200 km altitude in 90 min. This rate of vertical propagation matches the vertical phase speed computed through dispersion relation using wave frequency from spectral analysis and horizontal phase speed. The second case study involves simulation of topography induced GWs to generate cold pockets for CO_2 condensation. Periodicities in terrain are linked to periodicities in cold pockets formed by wave perturbations in temperature. The observed cloud echoes lie in the cold pockets and their slopes match those of the simulated cold pockets. This is explained by the fact that ice particles nucleate and sublimate successively as they advect through the temperature-modulated atmosphere. Lower computational overhead accorded by considering only two dimensions instead of three makes MAGNUS-P well suited for conducting iterative studies over a large parameter space. The model can be used to perform comparative studies of GW propagation, growth, and dissipation on different planets by varying the ambient atmospheric and solar activity characteristics.

Appendix A Molecular viscosity calculation

Banks and Kockarts (2013) provide power law expressions for molecular viscosity of different gas species as function of temperature in the form:

$$\nu_i = A_i T^{0.69}/\rho \tag{A1}$$

with coefficients $A_{O_2} = 4.03$, $A_{N_2} = 3.43$ and kinematic viscosity (ν) in g/cm/s. Using data from Golubev (1970) and performing curve fitting for power law of the same form, we obtain $A_{CO_2} = 3.38$ and $A_{Ar} = 4.49$. For gas mixtures, the equivalent coefficient can be evaluated using (Banks & Kockarts, 2013):

$$A = \frac{\Sigma A_i n_i}{\Sigma n_i} \tag{A2}$$

Here n_i is the mass fraction and A_i is the power law coefficient of individual species. For Earth, we take 78% N_2 and 22% O_2; For Mars: 95.5% CO_2, 2.6 % N_2 and 1.9 % Ar; For Venus: 96.5% CO_2 and 3.5% N_2, resulting in:

$$\begin{aligned} \nu_{Earth} &= 3.56 \times 10^{-7} T^{0.69}/\rho, \\ \nu_{Mars} &= 4.2 \times 10^{-7} T^{0.69}/\rho, \\ \nu_{Venus} &= 3.38 \times 10^{-7} T^{0.69}/\rho \end{aligned} \tag{A3}$$

The units of ν in Eq. (A3) are kg/m/s.

Acknowledgments

The authors acknowledge funding support from NTU startup grant a Cubesat for Earth Observations and DSO project ARCADE for this work. The data files associated with results presented in this paper are available at the Data Repository, NTU at `https://doi.org/10.21979/N9/VGYQ9M`. Data files for the purposes of review are attached as supplementary files in MATLAB .fig format.

References

Alexander, M., Geller, M., McLandress, C., Polavarapu, S., Preusse, P., Sassi, F., … others (2010). Recent developments in gravity-wave effects in climate models and the global distribution of gravity-wave momentum flux from observations and models. *Quarterly Journal of the Royal Meteorological Society*, *136*(650), 1103–1124.

Andrews, D. G., Holton, J. R., & Leovy, C. B. (1987). *Middle atmosphere dynamics* (No. 40). Academic press.

Artru, J., Ducic, V., Kanamori, H., Lognonné, P., & Murakami, M. (2005). Ionospheric detection of gravity waves induced by tsunamis. *Geophysical Journal International*, *160*(3), 840–848.

Baker, R. D., Schubert, G., & Jones, P. W. (2000). Convectively generated internal gravity waves in the lower atmosphere of Venus. part I: No wind shear. *Journal of the Atmospheric Sciences*, *57*(2), 184–199.

Banks, P. M., & Kockarts, G. (2013). *Aeronomy*. Elsevier.

Barnes, J. R. (1990). Possible effects of breaking gravity waves on the circulation of the middle atmosphere of Mars. *Journal of Geophysical Research: Solid Earth*, *95*(B2), 1401–1421.

Barrow, D. J., & Matcheva, K. I. (2013). Modeling the effect of atmospheric gravity waves on Saturns ionosphere. *Icarus*, *224*(1), 32–42.

Brissaud, Q., Martin, R., Garcia, R. F., & Komatitsch, D. (2016). Finite-difference numerical modelling of gravitoacoustic wave propagation in a windy and attenuating atmosphere. *Geophysical Journal International*, *206*(1), 308–327.

Cheng, A. F., Summers, M. E., Gladstone, G. R., Strobel, D. F., Young, L. A., Lavvas, P., … others (2017). Haze in Pluto's atmosphere. *Icarus*, *290*, 112–133.

Crisp, D. (1989). Radiative forcing of the Venus mesosphere: II. thermal fluxes, cooling rates, and radiative equilibrium temperatures. *Icarus*, *77*(2), 391–413.

DasGupta, A., Das, A., Hui, D., Bandyopadhyay, K. K., & Sivaraman, M. (2006). Ionospheric perturbations observed by the GPS following the December 26th, 2004 Sumatra-Andaman earthquake. *Earth, Planets and Space*, *58*(2), 167–172.

Drob, D. P., Emmert, J. T., Meriwether, J. W., Makela, J. J., Doornbos, E., Conde, M., … others (2015). An update to the horizontal wind model (HWM): The quiet time thermosphere. *Earth and Space Science*, *2*(7), 301–319.

Eckermann, S. D., Ma, J., & Zhu, X. (2011). Scale-dependent infrared radiative damping rates on mars and their role in the deposition of gravity-wave momentum flux. *Icarus*, *211*(1), 429–442.

England, S. L., Liu, G., Yiğit, E., Mahaffy, P. R., Elrod, M., Benna, M., … Jakosky, B. (2017). MAVEN NGIMS observations of atmospheric gravity waves in the Martian thermosphere. *Journal of Geophysical Research: Space Physics*, *122*(2), 2310–2335.

Fels, S. B. (1982). A parameterization of scale-dependent radiative damping rates in the middle atmosphere. *Journal of Atmospheric Sciences*, *39*(5), 1141–1152.

Franke, P. M., & Robinson, W. A. (1999). Nonlinear behavior in the propagation of atmospheric gravity waves. *Journal of the Atmospheric Sciences*, *56*(17), 3010–3027.

Fritts, D. C., & Alexander, M. J. (2003). Gravity wave dynamics and effects in the middle atmosphere. *Reviews of Geophysics*, *41*(1).

Fritts, D. C., Tsuda, T., Kato, S., Sato, T., & Fukao, S. (1988). Observational evidence of a saturated gravity wave spectrum in the troposphere and lower stratosphere. *Journal of Atmospheric Sciences*, *45*(12), 1741–1759.

Gavrilov, N. M., & Kshevetskii, S. P. (2014). Three-dimensional numerical simulation of nonlinear acoustic-gravity wave propagation from the troposphere to the thermosphere. *Earth, Planets and Space*, *66*(1), 1–8.

Golubev, I. F. (1970). *Viscosity of gases and gas mixtures: A handbook*. Israel Program for Scientific Translations.

Hickey, M. P., Walterscheid, R. L., & Schubert, G. (2000). Gravity wave heating and cooling in Jupiter's thermosphere. *Icarus*, *148*(1), 266–281.

Hinson, D. P., & Jenkins, J. M. (1995). Magellan radio occultation measurements of atmospheric waves on Venus. *Icarus*, *114*(2), 310–327.

Hocke, K., Schlegel, K., et al. (1996). A review of atmospheric gravity waves and travelling ionospheric disturbances: 1982–1995. In *Annales geophysicae* (Vol. 14, p. 917).

Hu, R., Cahoy, K., & Zuber, M. T. (2012). Mars atmospheric CO2 condensation above the north and south poles as revealed by radio occultation, climate sounder, and laser ranging observations. *Journal of Geophysical Research: Planets*, *117*(E7).

Imamura, T., & Ogawa, T. (1995). Radiative damping of gravity waves in the terrestrial planetary atmospheres. *Geophysical Research Letters*, *22*(3), 267–270.

Kaspi, Y., & Showman, A. P. (2015). Atmospheric dynamics of terrestrial exoplanets over a wide range of orbital and atmospheric parameters. *The Astrophysical Journal*, *804*(1), 60.

Kim, Y.-J., Eckermann, S. D., & Chun, H.-Y. (2003). An overview of the past, present and future of gravity-wave drag parametrization for numerical climate and weather prediction models. *Atmosphere-Ocean*, *41*(1), 65–98.

Kundu, P. K., & Cohen, I. M. (2002). Fluid mechanics.

Langtangen, H. P., & Linge, S. (2017). *Finite difference computing with PDEs: a modern software approach*. Springer Nature.

Laughman, B., Fritts, D., & Lund, T. (2017). Tsunami-driven gravity waves in the presence of vertically varying background and tidal wind structures. *Journal of Geophysical Research: Atmospheres*, *122*(10), 5076–5096.

Lefèvre, M., Spiga, A., & Lebonnois, S. (2020). Mesoscale modeling of Venus' bow-shape waves. *Icarus*, *335*, 113376.

LeVeque, R. J. (2002). *Finite volume methods for hyperbolic problems*. Cambridge University Press.

Lewis, S. R., Collins, M., Read, P. L., Forget, F., Hourdin, F., Fournier, R., … Huot, J.-P. (1999). A climate database for Mars. *Journal of Geophysical Research: Planets*, *104*(E10), 24177–24194.

Liu, J.-Y., Tsai, Y.-B., Ma, K.-F., Chen, Y.-I., Tsai, H.-F., Lin, C.-H., … Lee, C.-P. (2006). Ionospheric GPS total electron content (TEC) disturbances triggered by the 26 December 2004 Indian Ocean tsunami. *Journal of Geophysical Research: Space Physics*, *111*(A5).

Matcheva, K. I., Strobel, D. F., & Flasar, F. (2001). Interaction of gravity waves with ionospheric plasma: Implications for Jupiter's ionosphere. *Icarus*, *152*(2), 347–365.

McGouldrick, K., & Toon, O. B. (2008). Observable effects of convection and gravity waves on the Venus condensational cloud. *Planetary and Space Science*, *56*(8), 1112–1131.

Medvedev, A., & Klaassen, G. (2000). Parameterization of gravity wave momentum deposition based on nonlinear wave interactions: Basic formulation and sensitivity tests. *Journal of Atmospheric and Solar-Terrestrial Physics*, *62*(11), 1015–1033.

Medvedev, A. S., González-Galindo, F., Yiğit, E., Feofilov, A. G., Forget, F., & Hartogh, P. (2015). Cooling of the Martian thermosphere by CO2 radiation and gravity waves: An intercomparison study with two general circulation models. *Journal of Geophysical Research: Planets*, *120*(5), 913–927.

Mikhailova, G., Mikhailov, Y. M., & Kapustina, O. (2016). The December 26, 2004, tsunami on Sumatra island as a source of internal gravity waves in the Earths atmosphere. *Geomagnetism and Aeronomy*, *56*(5), 634–640.

Nappo, C. J. (2013). *An introduction to atmospheric gravity waves*. Academic press.

Occhipinti, G., Lognonné, P., Kherani, E. A., & Hébert, H. (2006). Three-dimensional waveform modeling of ionospheric signature induced by the 2004 Sumatra tsunami. *Geophysical Research Letters*, *33*(20).

Parish, H. F., Schubert, G., Hickey, M. P., & Walterscheid, R. L. (2009). Propagation of tropospheric gravity waves into the upper atmosphere of Mars. *Icarus*, *203*(1), 28–37.

Pettengill, G. H., & Ford, P. G. (2000). Winter clouds over the north Martian polar cap. *Geophysical Research Letters*, *27*(5), 609–612.

Picone, J., Hedin, A., Drob, D. P., & Aikin, A. (2002). NRLMSISE-00 empirical model of the atmosphere: Statistical comparisons and scientific issues. *Journal of Geophysical Research: Space Physics*, *107*(A12), SIA–15.

Pitteway, M., & Hines, C. (1963). The viscous damping of atmospheric gravity waves. *Canadian Journal of Physics*, *41*(12), 1935–1948.

Read, P. L., Lewis, S. R., & Vallis, G. K. (2018). Atmospheric dynamics of terrestrial planets. *Handbook of Exoplanets*, *144*, 2537–2557.

Rees, M. H. (1989). *Physics and chemistry of the upper atmosphere*. Cambridge University Press.

Sanchez-Lavega, A. (2010). *An introduction to planetary atmospheres*. CRC Press.

Sánchez-Lavega, A., Lebonnois, S., Imamura, T., Read, P., & Luz, D. (2017). The atmospheric dynamics of Venus. *Space Science Reviews*, *212*(3), 1541–1616.

Snively, J. B., & Pasko, V. P. (2008). Excitation of ducted gravity waves in the lower thermosphere by tropospheric sources. *Journal of Geophysical Research: Space Physics*, *113*(A6).

Spiga, A., González-Galindo, F., López-Valverde, M.-Á., & Forget, F. (2012). Gravity waves, cold pockets and CO2 clouds in the Martian mesosphere. *Geophysical Research Letters*, *39*(2).

Tobie, G., Forget, F., & Lott, F. (2003). Numerical simulation of the winter polar wave clouds observed by Mars Global Surveyor Mars Orbiter Laser Altimeter. *Icarus*, *164*(1), 33–49.

Torrence, C., & Compo, G. P. (1998). A practical guide to wavelet analysis. *Bulletin of the American Meteorological society*, *79*(1), 61–78.

Vadas, S. L., & Fritts, D. C. (2005). Thermospheric responses to gravity waves: Influences of increasing viscosity and thermal diffusivity. *Journal of Geophysical Research: Atmospheres*, *110*(D15).

Watkins, C., & Cho, J. Y. (2010). Gravity waves on hot extrasolar planets. I. propagation and interaction with the background. *The Astrophysical Journal*, *714*(1), 904.

Wu, Y., Smith, S. G. L., Rottman, J. W., Broutman, D., & Minster, J.-B. H. (2020). Time-dependent propagation of tsunami-generated acoustic–gravity waves in the atmosphere. *Journal of Atmospheric Sciences*, *77*(4), 1233–1244.

Yiğit, E., Medvedev, A. S., & Hartogh, P. (2015). Gravity waves and high-altitude CO2 ice cloud formation in the Martian atmosphere. *Geophysical Research Letters*, *42*(11), 4294–4300.

Yu, Y., & Hickey, M. P. (2007). Time-resolved ducting of atmospheric acoustic-gravity waves by analysis of the vertical energy flux. *Geophysical Research Letters*, *34*(2).

Zuber, M. T., Smith, D., Solomon, S., Muhleman, D., Head, J., Garvin, J., ... Bufton, J. (1992). The Mars Observer Laser Altimeter investigation. *Journal of Geophysical Research: Planets*, *97*(E5), 7781–7797.

Figure 12.

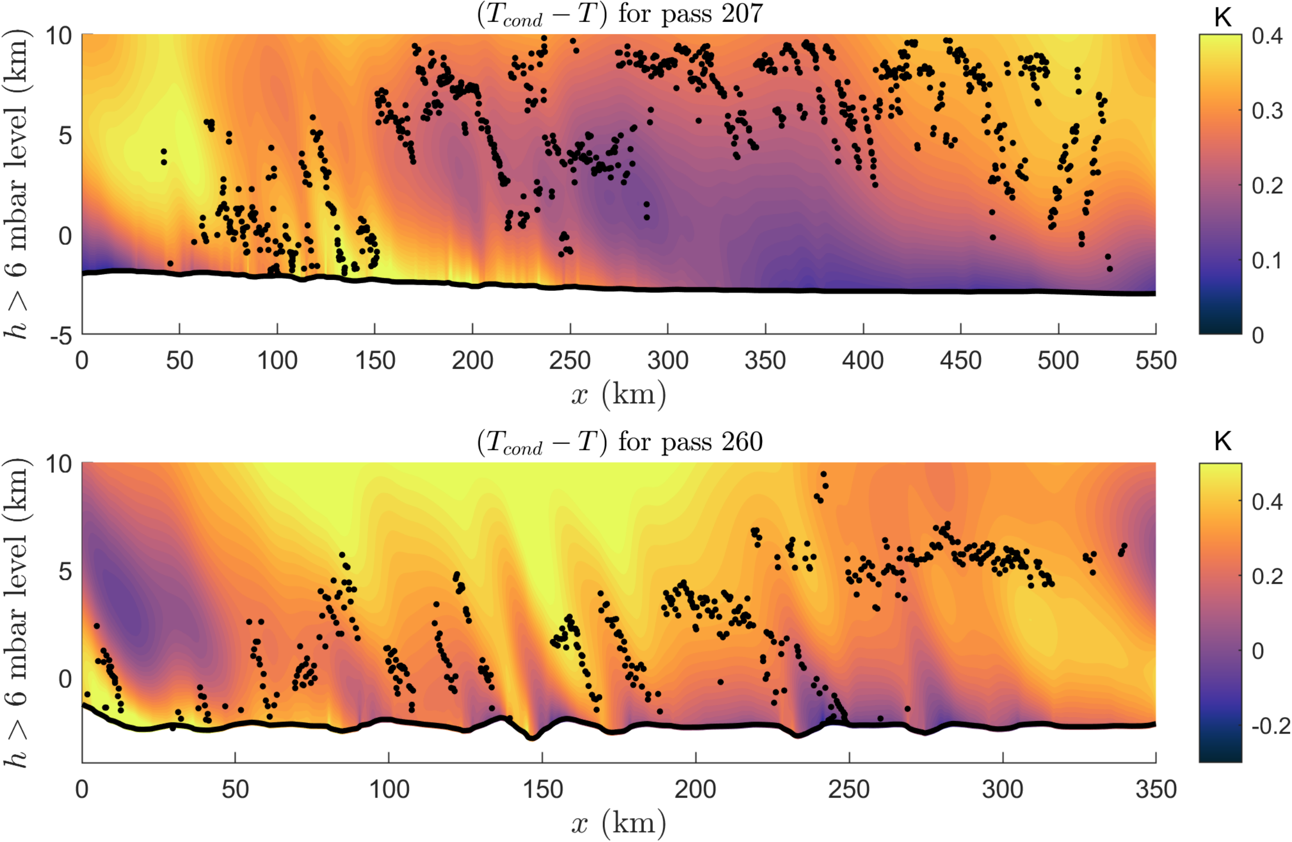

$(T_{cond} - T)$ for pass 207
$h >$ 6 mbar level (km)
10
5
0
-5
0
50
100
150
200
250
300
350
400
450
500
550
x (km)
K
0.4
0.3
0.2
0.1
0
$(T_{cond} - T)$ for pass 260
$h >$ 6 mbar level (km)
10
5
0
0
50
100
150
200
250
300
350
x (km)
K
0.4
0.2
0
-0.2

Figure 2.

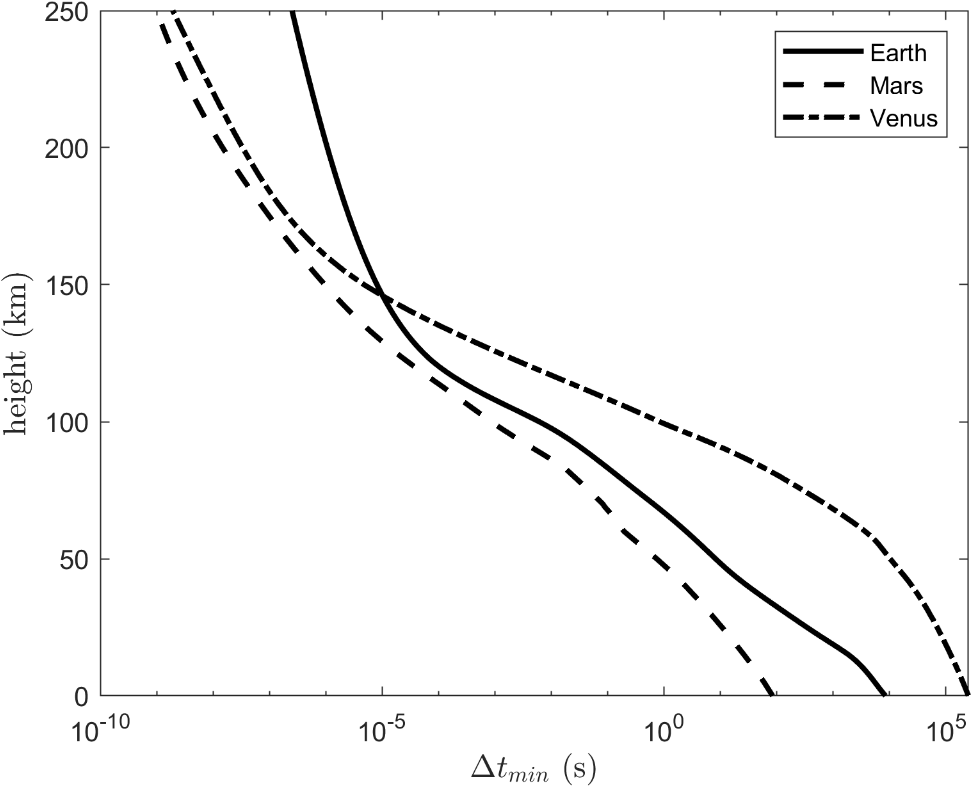

Earth
Mars
Venus
height (km)
250
200
150
100
50
0
10^{-10}
10^{-5}
10^{0}
10^{5}
Δt_{min} (s)

Figure 1.

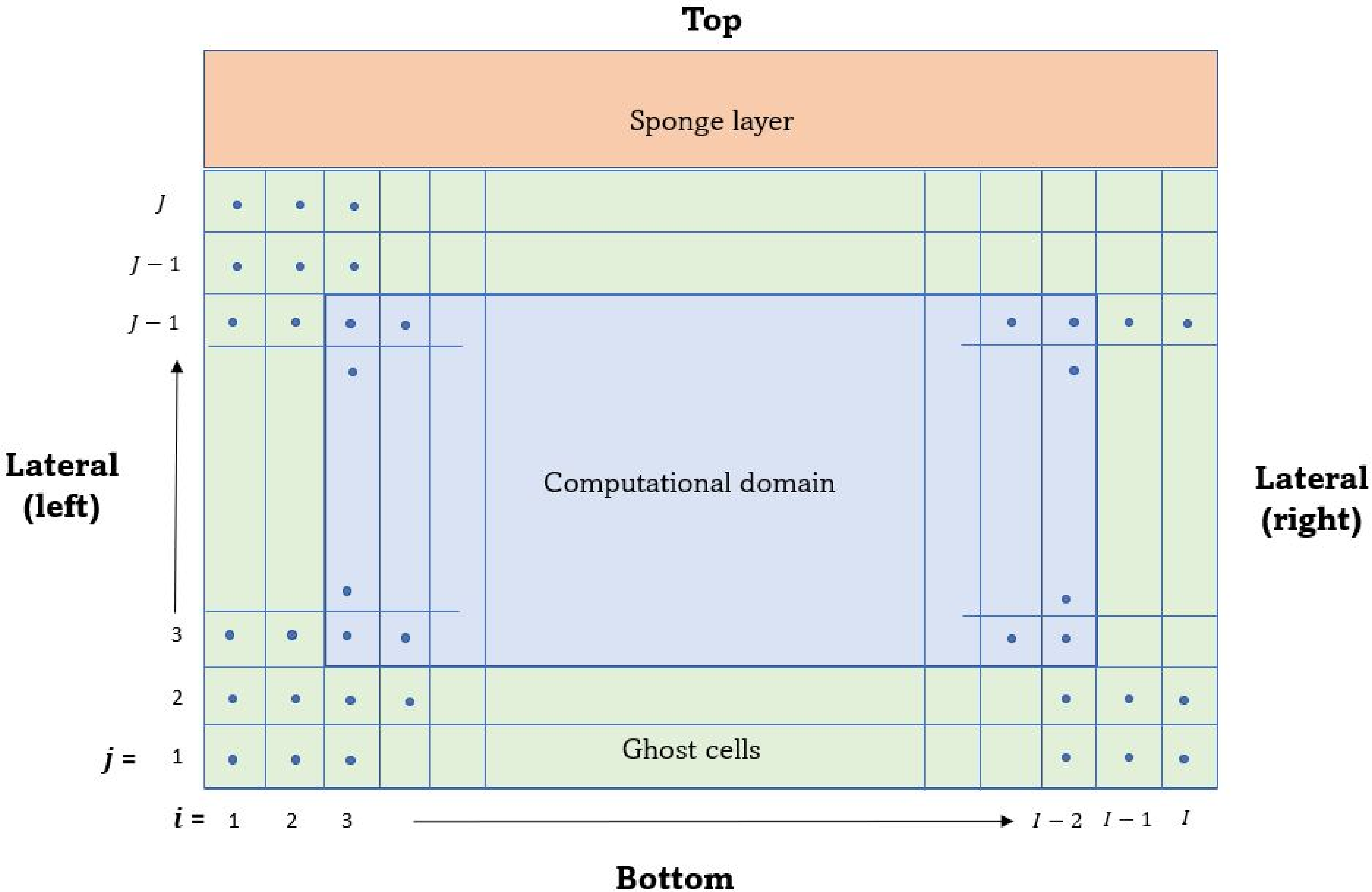

Top
Sponge layer
J
J − 1
J − 1
Lateral (left)
Computational domain
Lateral (right)
3
2
j = 1
Ghost cells
i = 1 2 3
I − 2 I − 1 I
Bottom

Figure 11.

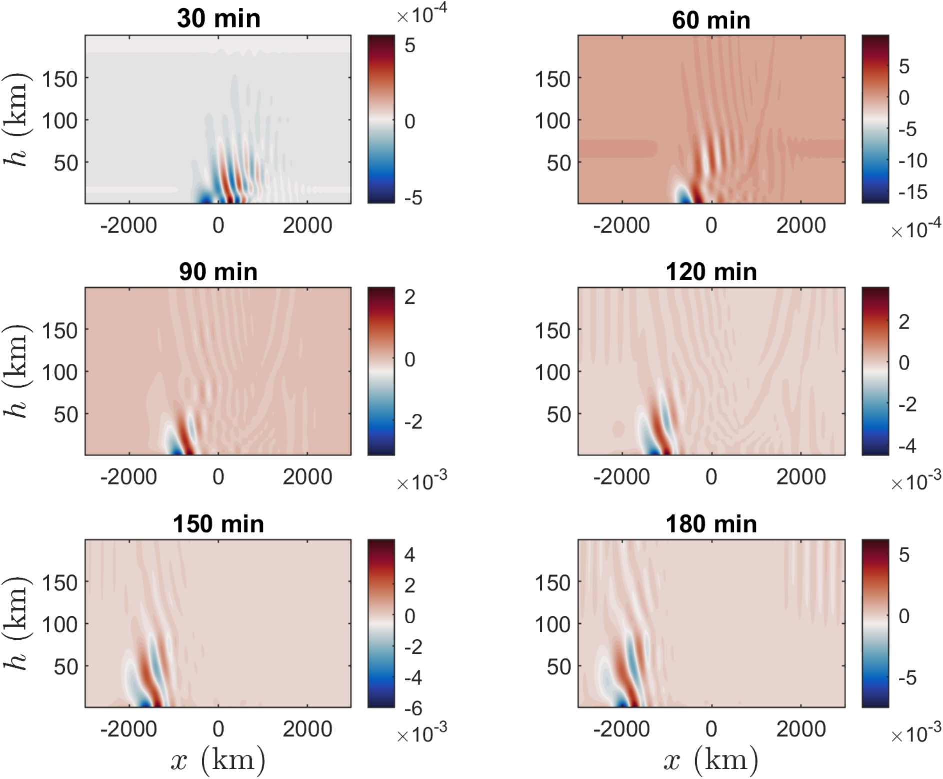

30 min
60 min
90 min
120 min
150 min
180 min
h (km)
x (km)
$\times 10^{-4}$
$\times 10^{-3}$
-2000
0
2000
150
100
50

Figure.

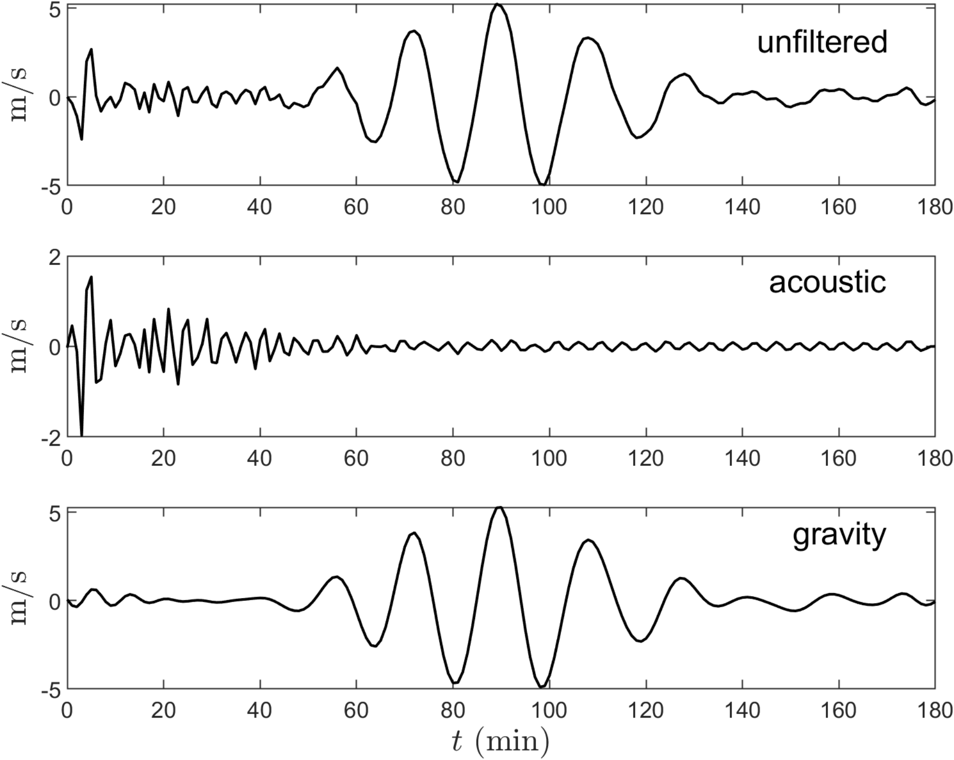

unfiltered
acoustic
gravity
m/s
5
0
-5
2
-2
0
20
40
60
80
100
120
140
160
180
t (min)

Figure 10.

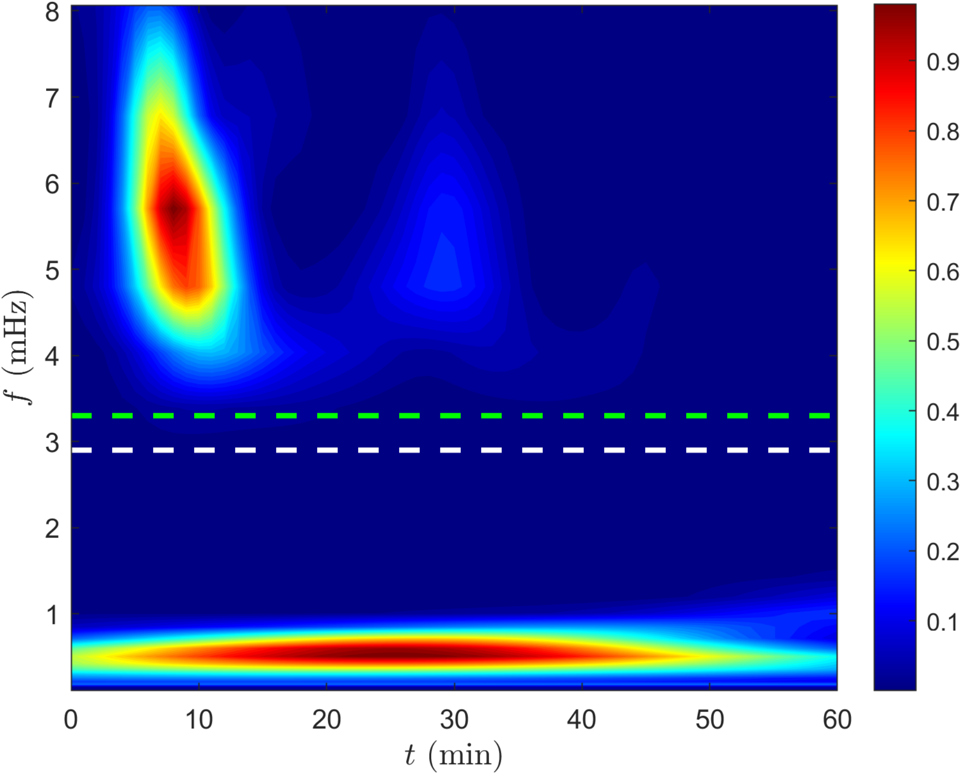
8
7
6
5
4
3
2
1
f (mHz)
0
10
20
30
40
50
60
t (min)
0.9
0.8
0.7
0.6
0.5
0.4
0.3
0.2
0.1

Figure 5.

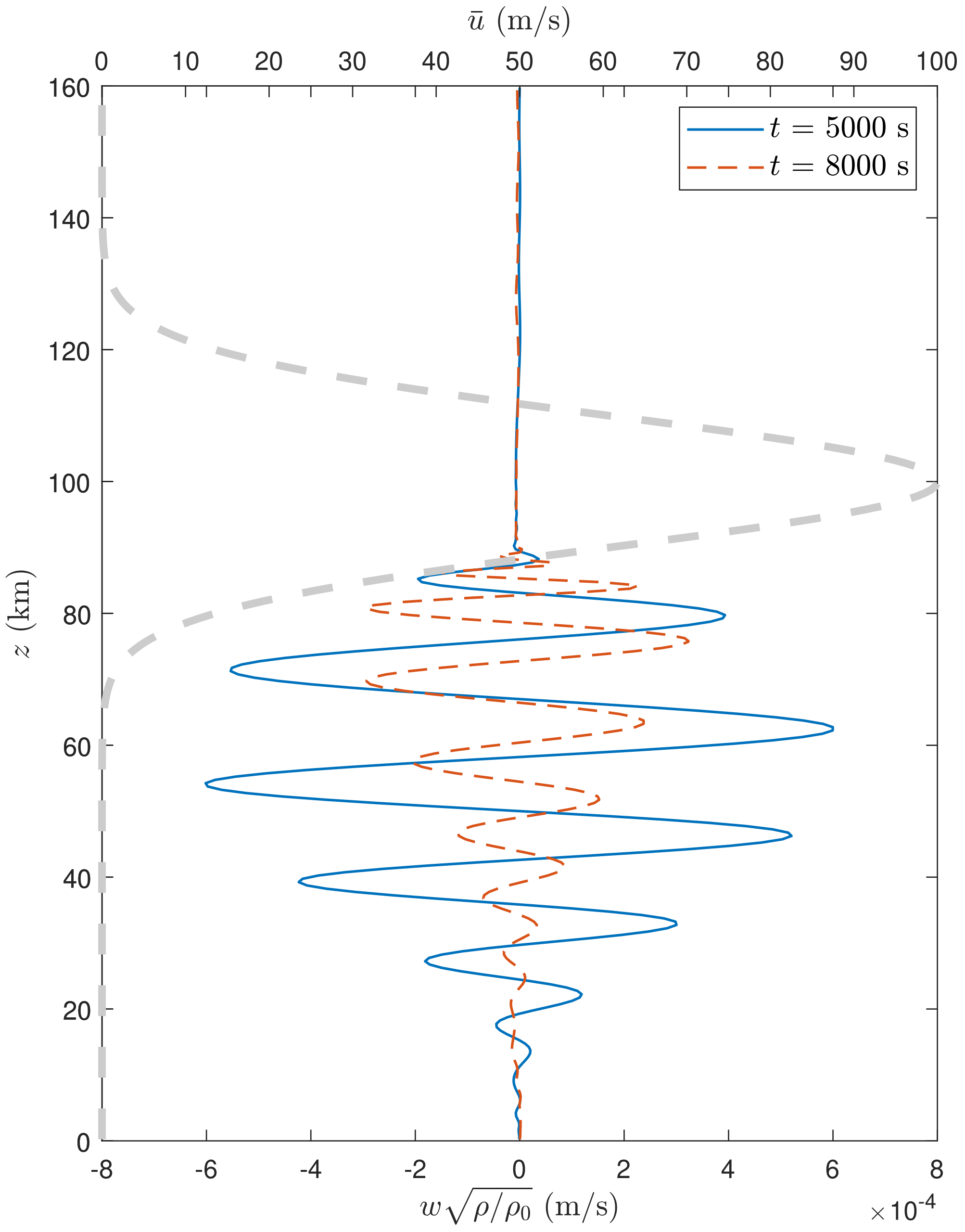

$\bar{u}$ (m/s)
0
10
20
30
40
50
60
70
80
90
100
160
140
120
100
80
60
40
20
0
z (km)
t = 5000 s
t = 8000 s
-8
-6
-4
-2
0
2
4
6
8
$w\sqrt{\rho/\rho_0}$ (m/s)
$\times 10^{-4}$

Figure 6.

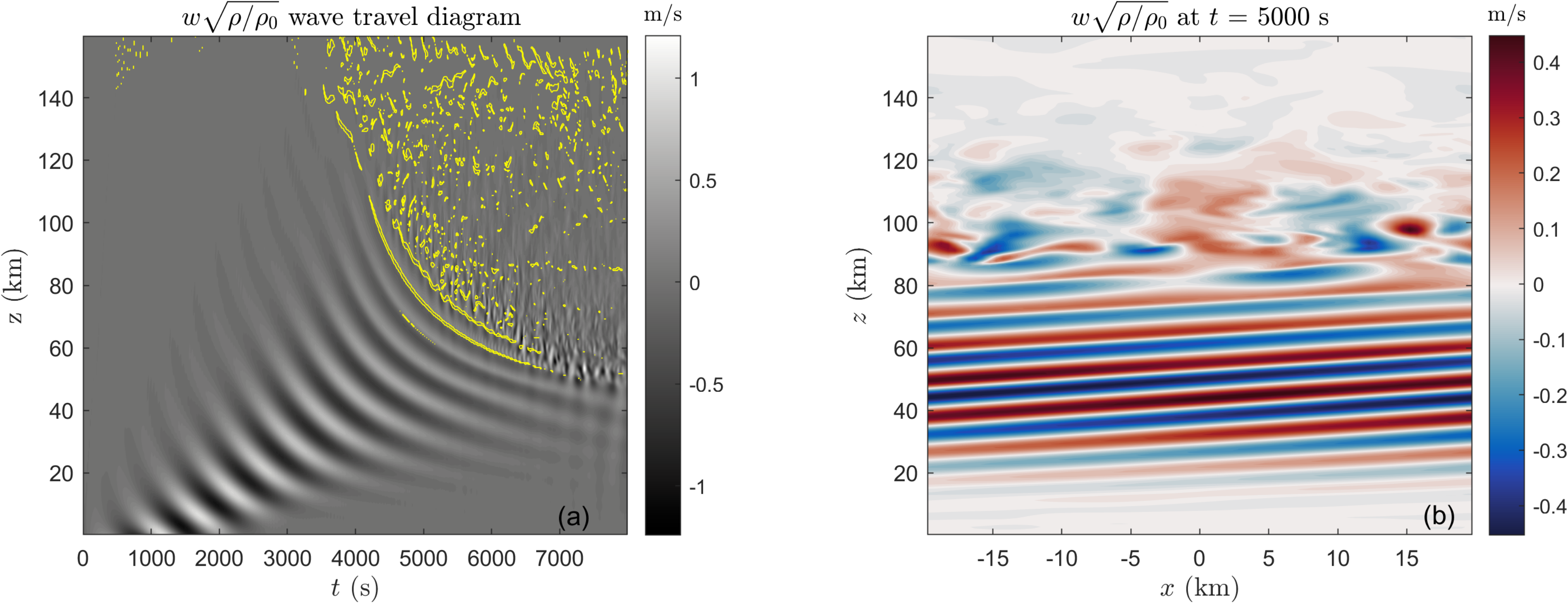

$w\sqrt{\rho/\rho_0}$ wave travel diagram
m/s
1
0.5
0
-0.5
-1
140
120
100
80
60
40
20
z (km)
0
1000
2000
3000
4000
5000
6000
7000
t (s)
(a)
$w\sqrt{\rho/\rho_0}$ at $t = 5000$ s
m/s
0.4
0.3
0.2
0.1
0
-0.1
-0.2
-0.3
-0.4
z (km)
-15
-10
-5
0
5
10
15
x (km)
(b)

Figure 4.

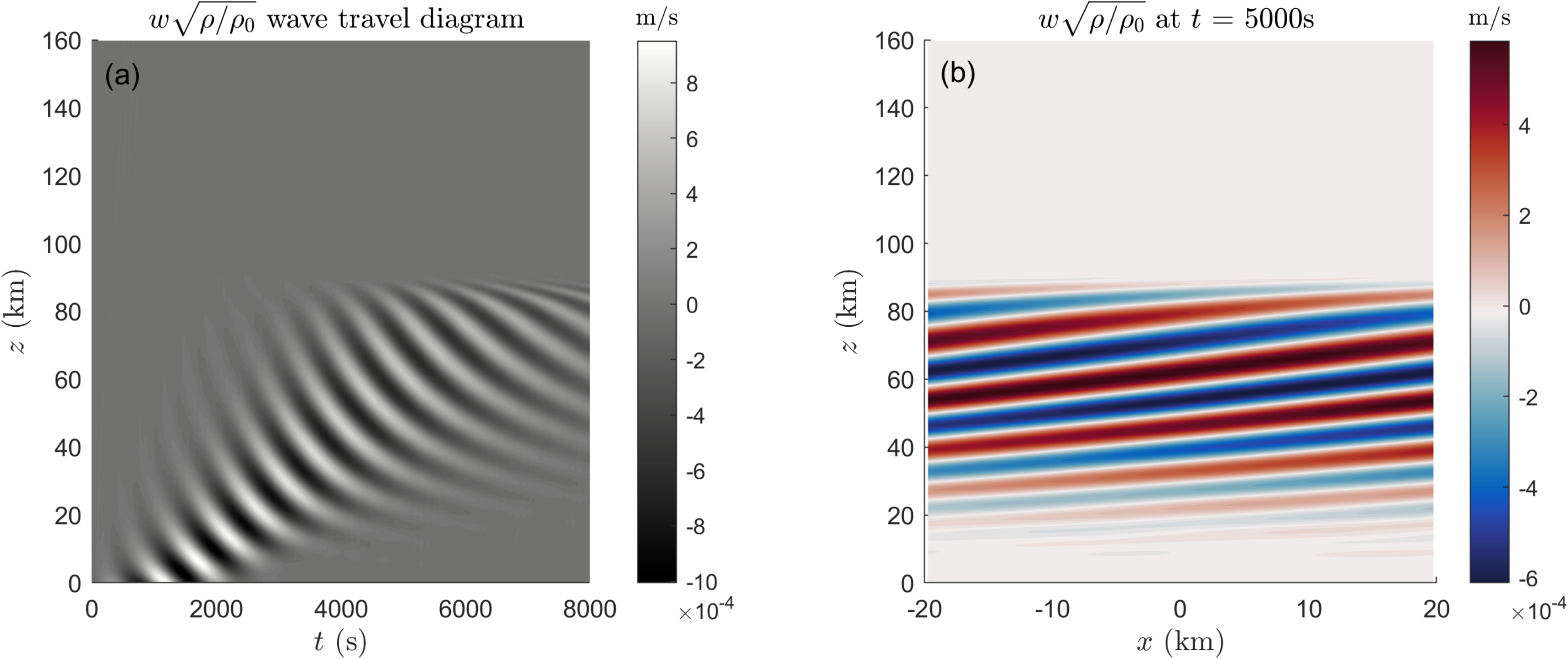

$w\sqrt{\rho/\rho_0}$ wave travel diagram
m/s
(a)
z (km)
t (s)
$\times10^{-4}$
$w\sqrt{\rho/\rho_0}$ at t = 5000s
m/s
(b)
z (km)
x (km)
$\times10^{-4}$

Figure 3.

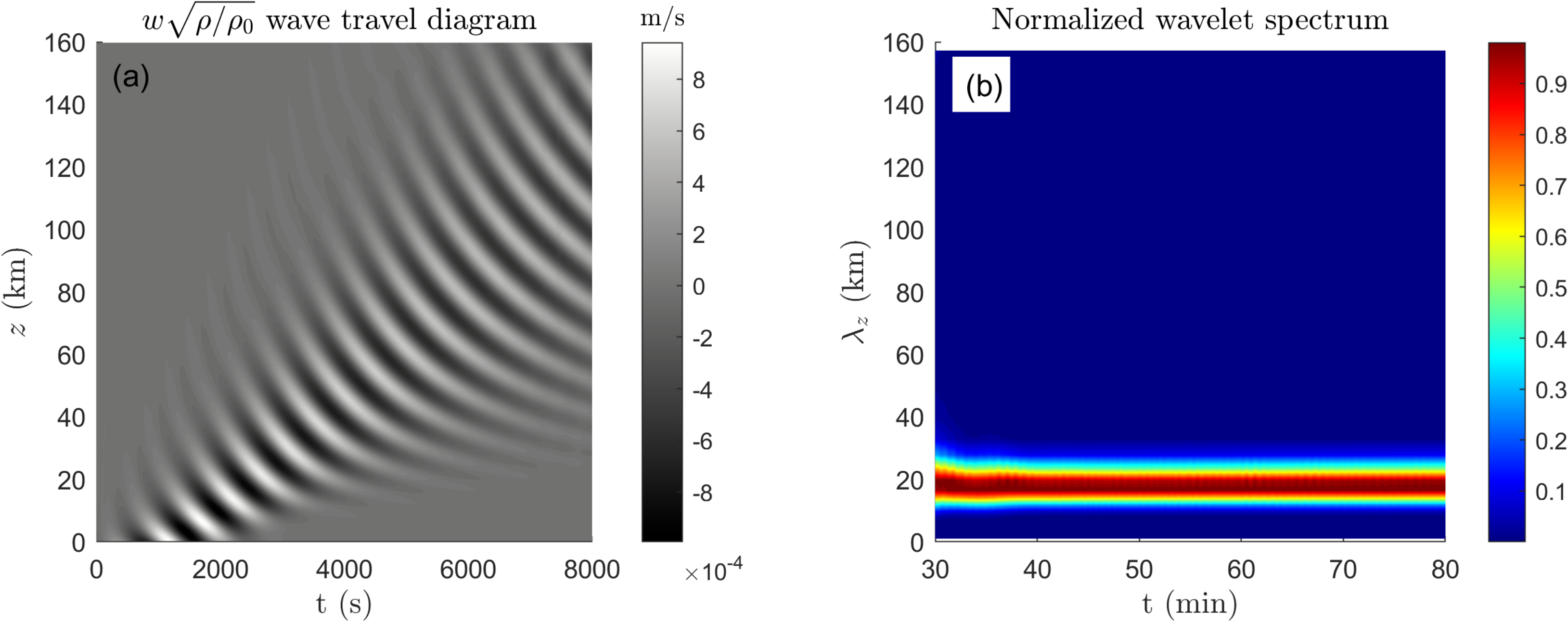

$w\sqrt{\rho/\rho_0}$ wave travel diagram
m/s
(a)
z (km)
t (s)
$\times 10^{-4}$
Normalized wavelet spectrum
(b)
λ_z (km)
t (min)

Figure 8.

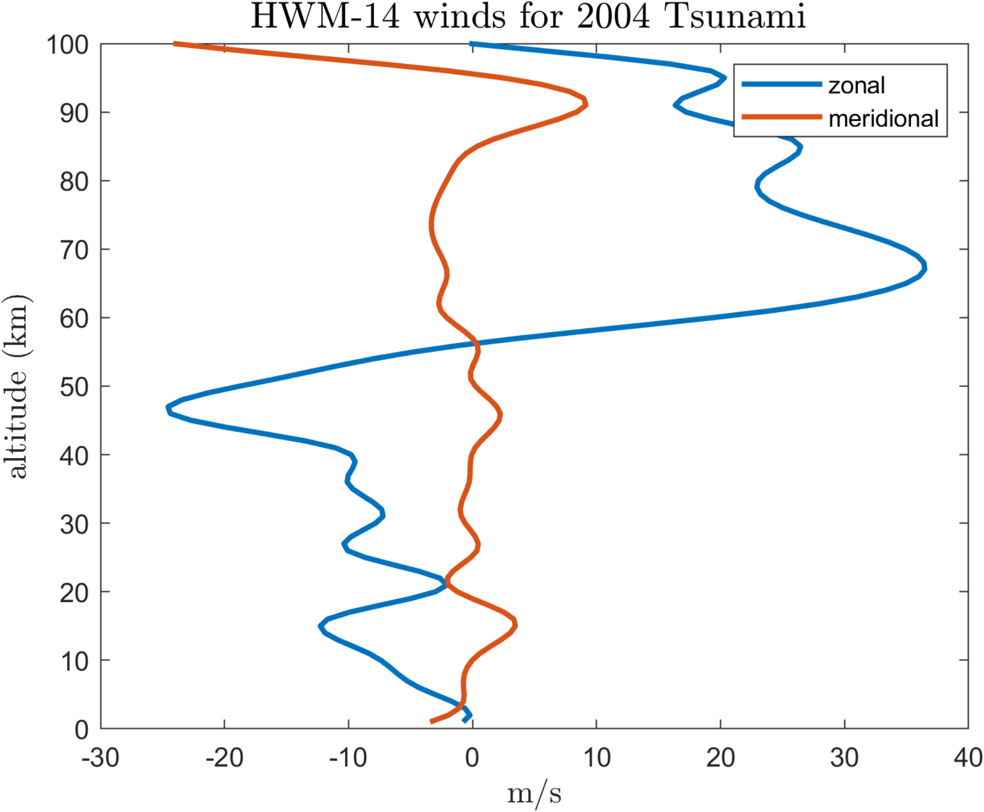
HWM-14 winds for 2004 Tsunami
zonal
meridional
altitude (km)
m/s
0
10
20
30
40
50
60
70
80
90
100
-30
-20
-10
0
10
20
30
40

Figure 7.

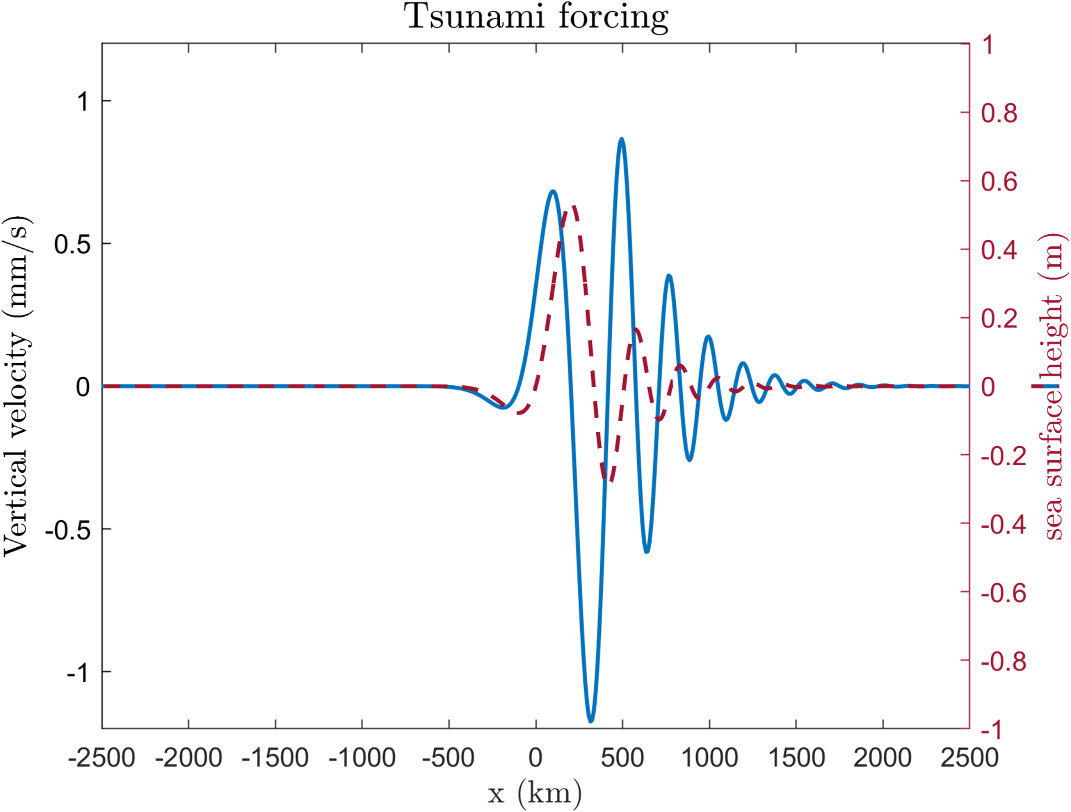
Tsunami forcing
Vertical velocity (mm/s)
sea surface height (m)
x (km)
1
0.5
0
-0.5
-1
0.8
0.6
0.4
0.2
-0.2
-0.4
-0.6
-0.8
-2500
-2000
-1500
-1000
-500
500
1000
1500
2000
2500